Journal of Bionic Engineering (2023) 20:2030–2043
https://doi.org/10.1007/s42235-023-00390-6

RESEARCH ARTICLE

A Soft Robotic Fish Actuated by Artificial Muscle Modules (SoRoFAAM-1)

Moise Raphael Tsimbo Fokou[1] · Qirong Xia[1] · Hu Jin[1] · Min Xu[1] · Erbao Dong[1]

Received: 16 December 2022 / Revised: 23 April 2023 / Accepted: 26 April 2023 / Published online: 24 July 2023

Abstract
In this paper, we present the design, fabrication, locomotion and bionic analysis of a Soft Robotic Fish Actuated by Artificial Muscle (SoRoFAAM). As a carangiform swimmer, the most important part of SoRoFAAM-1, on the motion point of view, is its tail designed around a bidirectional flexible bending actuator by layered bonding technology. This actuator is made of two artificial muscle modules based on Shape Memory Alloy (SMA) wires. Each artificial muscle module has four independent SMA-wire channels and is therefore capable of producing four different actuations. This design allows us to implement an adaptive regulated control strategy based on resistance feedback of the SMA wires to prevent them from overheating. To improve the actuation frequency to 2 Hz and the heat-dissipation ratio by 60%, we developed a round-robin heating strategy. Furthermore, the thermomechanical model of actuator is built, and the thermal transformation is analysed. The relationships between the actuation parameters and SoRoFAAM-1's kinematic parameters are analysed. The versatility of the actuator endows SoRoFAAM-1 with cruise straight and turning abilities. Moreover, SoRoFAAM-1 has a good bionic fidelity; in particular, a maneuverability of 0.15, a head swing factor of 0.38 and a Strouhal number of 0.61.

Keywords Soft robotic fish · Artificial muscle · Shape memory alloy · Head swing factor · Maneuverability · Bionic fidelity

1 Introduction

Fish locomotion modes are usually classified with respect to the fin(s) used to produce the thrust. In this classification, it turns out that, Body and/or Caudal Fin (BCF) and Median and/or Paired Fin (MPF) modes are the most dominant [1, 2]. BCF locomotion is used by approximately 85% of fish species and is further devised into anguilliform, subcarangiform, carangiform, thunniform and ostraciiform [3]. These swimming modes differ from each other by the wave-length of the wave travelling the fish while swimming. Carangiform, characterized by a wavelength between 4/3 and 4 BL (body length), is the most dominant [2]. Our goal in designing SoRoFAAM-1 was to considerably reduce the gap between living fish and robotic fish, that is why we have chosen to design it as a carangiform swimmer (keeping in mind it is the most dominant form). The qualitative measurement of our design goal was set as the degree of bionic fidelity of SoRoFAAM-1.

For the last two decades, robotic fish have attracted increasing attention from researchers. This increasing attention has its roots in two facts, that is, the inadequacy of some biological experimentation platforms and the engineering design challenge. In fact, the scientific investigation of fish swimming locomotion by biologists is traced back to 1933 and considerable progress has been made over time [2]. However, many fundamental questions remain opened [4]. The difficulty faced by biologists to answer most of these questions, despite the currently sophisticated experimental available setups, is the inherent coupling among parameters influencing features of interest. In fact, this makes it very difficult to isolate one parameter from the others and analyse its effect on the feature of interest. In this regard, robotic fish (or more desirable soft-robotic fish) have become a valuable experimental platform for biologists and in general for scientists interested in fish swimming hydrodynamics [5–8].

The second fact, that is the engineering design challenge of biomimetic robotic fish, is related to the fact that living fish achieve very high swimming efficiency

✉ Erbao Dong
ebdong@ustc.edu.cn

[1] CAS Key Laboratory of Mechanical Behavior and Design of Materials, Department of Precision Machinery and Precision Instrumentation, University of Science and Technology of China, Hefei 230026, China

compare to their robot counterparts. In addition, our traditional actuators are useless when a robot has to be biomimetic because of their rigidity, bulkiness, noise and lack of compliance. As a result, one has to rely on soft and smart materials that have been shown to be multifunctional [9] and capable of easily mimicking animals [1, 2, 10, 11]. However, the issue with these smart materials is their nonlinearity and hysteresis (in most cases), which tremendously increase the complexity of the modelling and control design phases.

Several soft robotic fishes have been developed in the last decade with smart-material-based actuators, such as ionic polymer-metal composites [12, 13], dielectric elastomers [10, 14–16], fluidic elastomers [17, 18] and Shape Memory Alloy (SMA) wires [19, 20]. Compared to robotic fishes using traditional actuators, smart materials endow these soft robots with compactness, flexibility, light weight and multimode movement. However, the bionic fidelity of most of these soft robotic fishes is not satisfactory.

The advantage of SMA-based actuators over most smart-material-based actuators is their high power density and actuation stress [21]. However, in general they have low permissible actuation frequency and recoverable strain. Since high flapping frequency is not required in BCF locomotion, the former is not an issue. The most significant issue resides in the thermal/mechanical hysteresis and the nonlinear phase transformation, which make the design of a controller difficult [22]. Some works have been done in this regard by using algorithms [23, 24], pulse width modulation [25] or SMA resistance feedback with neural networks [26]. However, these control strategies of SMA-based actuators rely on the intermediate states of SMA, which are unpredictable and unreliable, limiting their performances. In this paper, we use our previous control strategy, viz. the Adaptive Regulated (AR) strategy [27], and we develop a new heating scheme, viz. the Round Robin heating strategy, to improve the actuation performance. Both schemes do not suffer from the previously mentioned limitations; thus, they can produce four independent accurate bending amplitudes without concern for the intermediate states of SMA wires and rely only on the final state, which is reliable.

The objective of this paper is to design a soft robotic fish based on artificial muscle modules with high bionic fidelity, especially on the muscle-skeleton-nerve impulse control mechanism. Table 1 shows the design specifications of SoRoFAAM-1 in terms of well-known swimming hydrodynamic parameters of living fishes. We begin by the design and fabrication of SoRoFAAM-1 in Sect. 2. Then in Sect. 3, we build the thermomechanical model of the bidirectional flexible bending actuator to analyse its bending characteristics and its thermodynamic behavior. In Sect. 4 we analyse two swimming patterns of SoRoFAAM-1, i.e. cruise straight and turning. Then we evaluate its bionic fidelity by means of its Strouhal number, head swing factor and maneuverability. In the last section we conclude and give some perspectives.

Table 1 Design specifications of SoRoFAAM-1 in terms of swimming hydrodynamic parameters of living fishes

Symbol	Description	Specification
S_h	Head swing factor	$0.15 \leq S_h \leq 0.4$
S_t	Strouhal Number	$0.25 \leq S_t \leq 0.4$
M_r	Maneuverability from rest	$M_r \leq 0.5$

2 Design and Methods

2.1 Design and Fabrication of the Bidirectional Flexible Bending Actuator Based on Artificial Muscle Modules

The bidirectional flexible bending actuator, which we will call actuator for short subsequently, consists of three layers, a spring steel sheet and two artificial muscle modules. The key component in these artificial muscle modules is an actuator skeleton consisting of two printed circuit boards and SMA wires (Fig. 1a). The SMA wires are arranged in four independent channels, from C_i (i = 1, 2, 3, 4) to GND(ground). As we will see later in this section, depending on the number of heated SMA wires, this arrangement endowed any artificial muscle of four independent actuations. To fabricate the artificial muscle module, the actuator skeleton is put in a mould, the PDMS (polydimethylsiloxane) is poured into the mould (Fig. 1b). An oven is used to reduce the curing time of the PDMS. After curing, the artificial muscle module is demoulded (Fig. 1c). An adhesive glue (HS-862 made by Anybond and A770 made by XYS HBOND as activation agent) is then applied to symmetrically bond both artificial muscle modules via a spring steel sheet to obtain the bidirectional flexible actuator (Fig. 1d and e). Each artificial muscle is responsible for bending the actuator in one direction; while, the other artificial muscle and the spring steel provide a restoring moment.

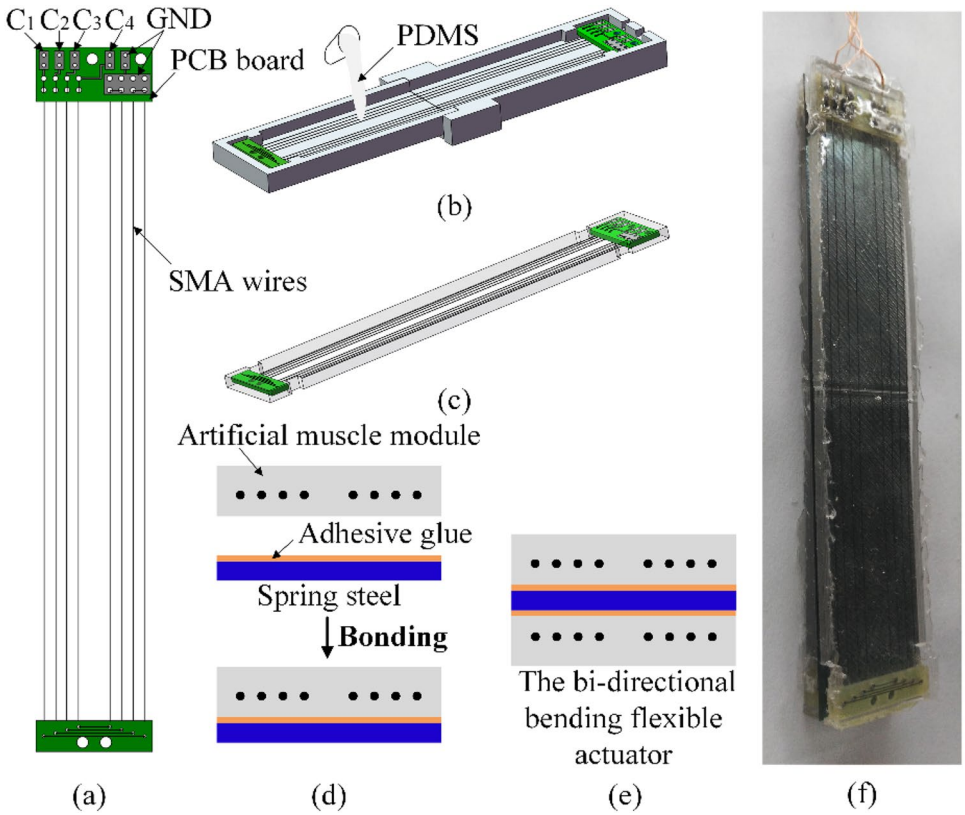

Fig. 1 Design and fabrication of the actuator. **a** Actuator skeleton. **b** Fabrication of an artificial muscle module. **c** 3D model of the artificial muscle module. **d** Bonding process of the components. **e** Cross view of the actuator. **f** Final prototype of the bi-directional flexible actuator

2.2 Design and Fabrication of SoRoFAAM-1

For the reasons stated earlier, SoRoFAAM-1 (Soft Robotic Fish Actuated by Artificial Muscle 1) mimics BCF swimmers, especially carangiform swimmers. As a consequence, its head and tail are two-third and one-third, respectively, of the main body length. The tail is responsible for producing the thrust and is mainly made up of the bidirectional flexible bending actuator. As shown in Fig. 2a, one end of the actuator is joined to the anterior portion via a hollow so that SoRoFAAM-1 will swim smoothly. A tail fin is cut from 1 mm-thick silicone pad and joint to the other end of the actuator. The actuator is then cast with silicone rubber (Ecoflex™ 00–10 made by Smooth-on) inside two injection moulds (Fig. 2b and c). Both parts A and B of the silicone rubber are first well stirred separately then mixed together at a 1:1 weight ratio. The mixture is placed in a vacuum chamber for degassing prior to mould it. Figure 2d shows SoRoFAAM-1, with dimensions of $\boldsymbol{Lh} = 160$ mm, $\boldsymbol{Lb} = 80$ mm and $Lf = 40$ mm.

2.3 Heating Strategy of the Bi-directional Flexible Bending Actuator

It is known that by varying the heating frequency, SMA wires exhibit different behaviors [8]. As a result, it is very important to accurately control the heating and cooling processes in order to obtain desired responses from SMA-based actuators. However, it is difficult to do so because of the nonlinearity and lag in SMA phase transformation process. For this reason, we use the AR heating strategy to obtain several bending ranges yet preventing overheating, as described next.

The resistance of a SMA wire exhibits a rapid fluctuation during the phase transformation process. By connecting a precise resistor in series with the SMA wire, SMA wire resistance fluctuations can be detected by means of the voltage variation across the series resistor. From the voltage divider rule:

$$V_{sample} = \frac{R_{sample}}{R_{sample} + R_{SMA}} V_S \tag{1}$$

where $\boldsymbol{R}_{\mathbf{SMA}}$ is the resistance of SMA wires, $\boldsymbol{V}_{\mathbf{S}}$ is the supply voltage, $\boldsymbol{V}_{\mathbf{sample}}$ is the voltage across the series resistor and $\boldsymbol{R}_{\mathbf{sample}}$ its resistance.

The supply voltage is kept constant at 22 V for a heating time of 400 ms. Figure 3 shows the evolution of the voltage across the series resistor. Point S and F correspond to the starting and endpoints, respectively, of the reverse martensitic transformation. The heating process must be stopped around point F to avoid overheating the actuator. Otherwise, the actuation ability will decrease.

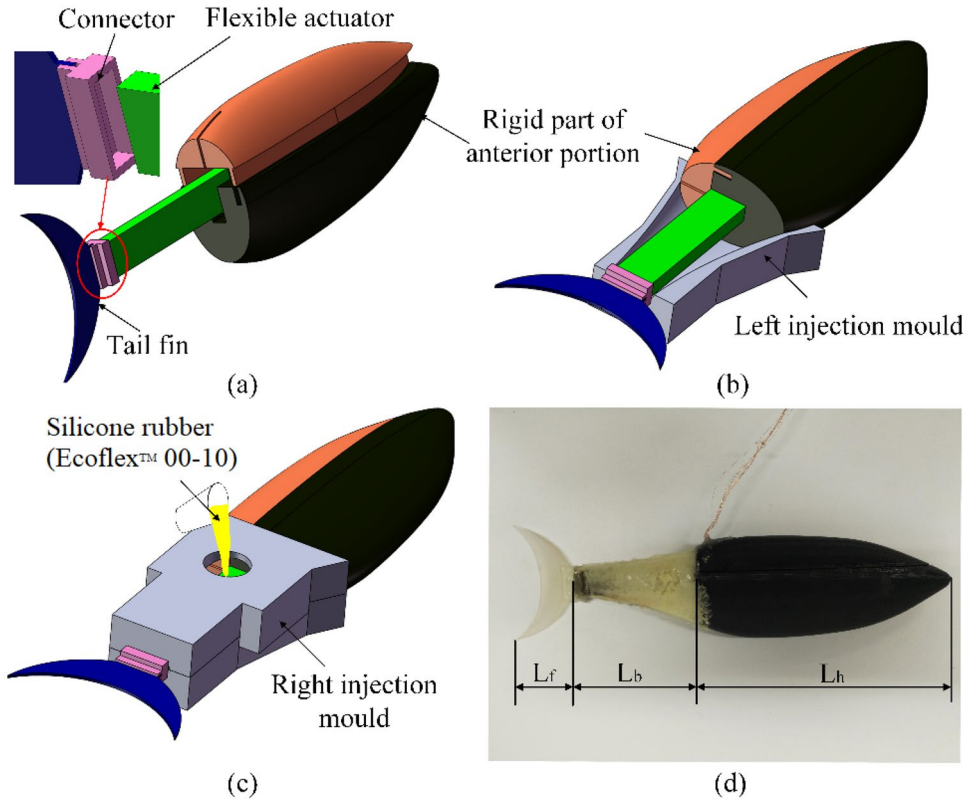

Fig. 2 Design and fabrication of SoRoFAAM-1. **a** 3D CAD Skeleton assembling. **b** Insertion in an injection mould for casting. **c** Tail moulding with silicone rubber. **d** Final prototype of SoRoFAAM-1

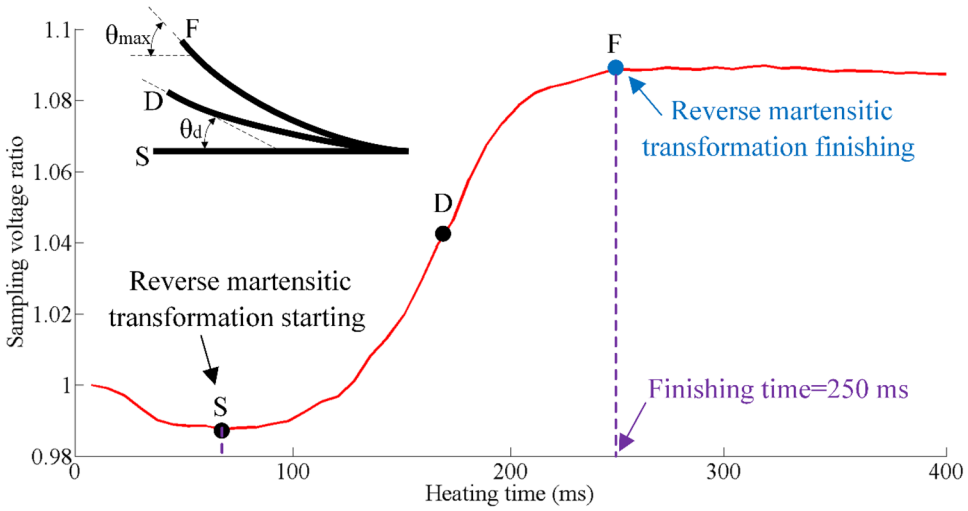

Fig. 3 Sample voltage variation because of SMA-wire resistance variation during heating

Let R_{max} and R_{min} been the resistances of the SMA wire at points S and F, respectively. Then, the resistance of an arbitrary point between S and F is $R(\tau) = R_{max} - (R_{max} - R_{min}) * \tau$, $\tau \in [0,1]$ is the resistance ration coefficient**.** By heating different number of channels of SMA wire with the AR heating strategy, we obtain four groups of response of the actuator (Fig. 4). When**,** the SMA wires reach the end of the phase transformation (point F in Fig. 3) and the bending angle is accurately known, reliable and stable. However, for $\tau \neq 1$, i.e., the SMA wires are in a thermal intermediate state, the bending range is unreliable. In addition, the Fig. 4 shows that, the AR heating strategy leads to a quasi-linear relationship between the bending amplitude and the resistance of SMA wire. Moreover, AR strategy provides at $\tau = 1$ four accurate bending amplitudes, unlike those obtained at intermediate states (large error). However, the AR strategy does not improve the heating frequency. Thus it is only suitable for low actuation frequencies.

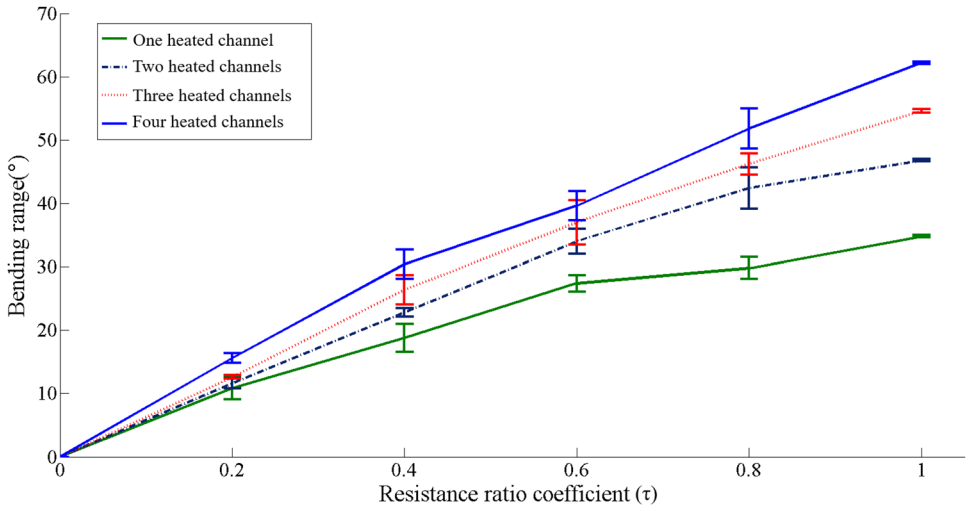

Fig. 4 Bending angle of the actuator as a function of the resistance ratio coefficient τ

3 Modelling and Simulation

3.1 Bending Model of the Bidirectional Flexible Bending Actuator

Because of the complexity in modelling the SMA wires and hence the actuator, we make the following assumptions: (1) the bent shape of the actuator is circular. (2) The horizontal bisector plan of the spring steel sheet is the neutral surface of the actuator, and the distance D between SMA wires and the neutral surface is constant during bending. (3) The temperature variation within the PDMS is too small and can be neglected. The parameters of the actuator model are listed in Table 2.

Figure 5 shows the mechanical model of the actuator. The bending radius of the neutral surface is R, and its bending angle is θ (Fig. 6a). From assumption 1, they are related by $\theta = L/R$, where L is the length of the actuator. To verify the consistency of this assumption, we have measured the distance from O to points B, C and D for various bending

Table 2 The parameters in the model of the bi-directional flexible actuator

Description (parameters)	Value (unit)
Length of the bi-directional flexible bending (L) actuator (L)	80 mm
Distance between SMA wires and neutral surface (D)	1 mm
Thickness of spring steel sheet (hs)	0.1 mm
Thickness of PDMS (hp)	2.7 mm
Maximum residual strain($\boldsymbol{\varepsilon_L}$)	4.3%
Width of the bi-directional flexible bending actuator (b)	17 mm
Young's modulus of spring steel sheet (E_S)	200 GPa
Young's modulus of PDMS (E_P)	5 MPa
Austenitic Young's modulus of SMA-wire (E_A)	83 GPa
Martensitic Young's modulus of SMA-wire (E_M)	28 GPa
The number of SMA wires(n)	8
SMA initial martensitic fraction ($\boldsymbol{\varepsilon_0}$)	1
Austenite start temperature (A_s)	71.5℃
Austenite finish temperature (A_f)	79.7℃
Martensitic start temperature (M_s)	54.5℃
Martensitic finish temperature (M_f)	41.4℃
Effect of stress on austenite temperature (C_A)	12 MPa/℃
Effect of stress on martensitic temperature (C_M)	10 MPa/℃
Density of SMA wires($\boldsymbol{\rho_{SMA}}$)	6.45 g/cm^3
Specific heat capacity ($\boldsymbol{c_{SMA}}$)	837 J/(kg·℃)
Latent heat of transformation (H)	24.3×10^3 J/kg

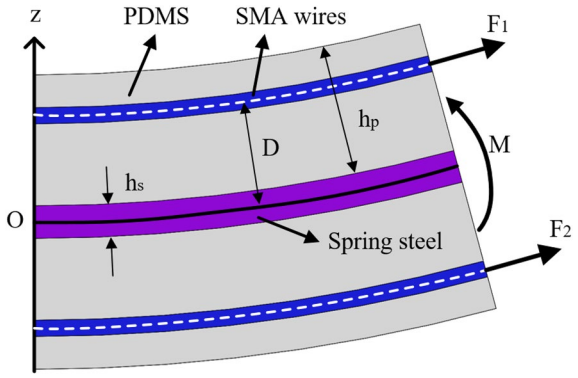

Fig. 5 The mechanical model of the bi-directional flexible actuator

angle (Fig. 6a). Figure 6b it shows that OB, OC and OD are almost equal regardless of the bending angle. Therefore, our assumption is quite valid, i.e., the actuator has a circular shape when bending. The curvature K can be approximately expressed as

$$K = \frac{1}{D}(\varepsilon_L - \varepsilon_{SMA}) \tag{2}$$

where $\boldsymbol{\varepsilon_{SMA}}$ is the SMA wires strain and $\boldsymbol{\varepsilon_L}$ is its maximum residual. When the actuator is in equilibrium, the net moment of any differential element (Fig. 5) is null:

$$\sum M_N = F_1 D - F_2 D - M = 0 \tag{3}$$

where M is the moment exerted on the PDMS and is given by

$$M = \int_{-h_s/2}^{h_s/2} E_s b K z^2 dz + \int_{h_s/2}^{h_s/2+h_p} E_p b K z^2 dz + \int_{-(h_s/2+h_p)}^{-h_s/2} E_p b K z^2 dz \tag{4}$$

From (3) and (4) it comes that

$$F_1 = \left(\int_{-h_s/2}^{h_s/2} E_s b K z^2 dz + \int_{h_s/2}^{-h_s/2+h_p} E_p b K z^2 dz + \int_{-(h_s/2+h_p)}^{-h_s/2} E_p b K z^2 dz + F_2 D \right) / D \tag{5}$$

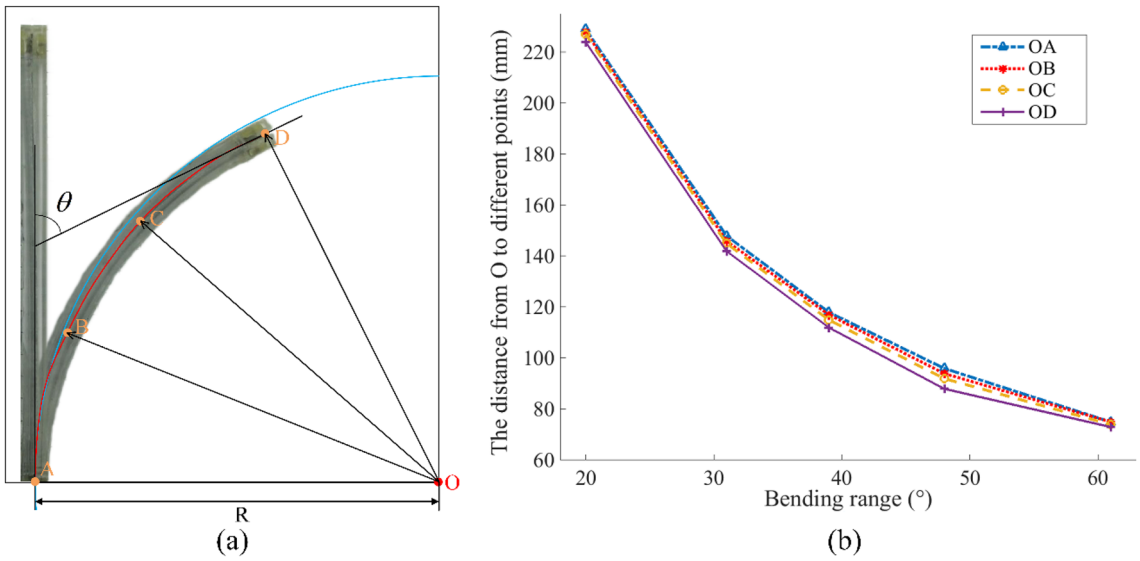

Fig. 6 Arc fitting of the bi-directional flexible actuator. **a** Schematic of the arc fitting. **b** Distance from O to A (fixed end), B, C and D (free end) as a function of the bending range

F_1 is the resultant force on the heated SMA wires and F_2 the pulling force on the unheated SMA wires.

$$F_2 = nE_M DK\pi d_{SMA}^2/4 \tag{6}$$

Using $\boldsymbol{F_1} = \boldsymbol{\sigma_{SMA}} \boldsymbol{A_{SMA}}$ and $\boldsymbol{\sigma_{SMA}} = \boldsymbol{k}\left(\boldsymbol{\varepsilon_L} - \boldsymbol{\varepsilon_{SMA}}\right)$, from Eqs. (2), (5) and (6):

$$\boldsymbol{k} = \left(\frac{\boldsymbol{E_s h_s^3 b}}{12\boldsymbol{D}} + \frac{2\boldsymbol{E_P}}{3}\left[\left(\frac{\boldsymbol{h_s}}{2} + \boldsymbol{h_p}\right)^3 - \left(\frac{\boldsymbol{h_s}}{2}\right)^3 + \frac{\boldsymbol{nE_M} \mathrm{D}\pi \boldsymbol{d_{SMA}^2}}{4}\right]\boldsymbol{b}\right)\frac{1}{\boldsymbol{D}}\frac{1}{\boldsymbol{A_{SMA}}} \tag{7}$$

The essence of SMA wires actuation is the transformation between austenite and martensite phases [21]. When SMA wires are heated to a temperature higher than the austenite start temperature A_s, they will transform from the martensite phase to the austenite phase, while producing a shrinkage and/or force. From the simplified Liang-rogers model of SMA constitutive models [28]:

$$\dot{\sigma}_{SMA} = E(\epsilon)\left(\dot{\varepsilon}_{SMA} - \varepsilon_L \dot{\epsilon}\right) \tag{8}$$

where $E(\epsilon)$ is the Young's modulus of SMA wires and $\boldsymbol{\epsilon}$ is the martensite fraction. They are related by $\boldsymbol{E}(\boldsymbol{\epsilon}) = \boldsymbol{E_A} + \boldsymbol{\epsilon}(\boldsymbol{E_M} - \boldsymbol{E_A})$. The martensite fraction during heating is given by:

$$\epsilon = \frac{\epsilon_0}{2} cos\left[a_A\left(T - A_s\right) + b_A \sigma_{SMA}\right] + \frac{\epsilon_0}{2}, A_s + \frac{\sigma_{SMA}}{C_A} \leq T \leq A_f + \frac{\sigma_{SMA}}{C_A} \tag{9}$$

where $a_A = \pi/(A_f - A_s), b_A = -a_A/C_A$. The thermal model of SMA wires can be expressed by:

$$\rho_{SMA} V_{SMA} c_{SMA} \dot{T} = i_{SMA}^2 R_{SMA} - hS_{SMA}(T - T_{na}) + \rho_{SMA} V_{SMA} H\dot{\epsilon} \tag{10}$$

where $\boldsymbol{S_{SMA}}$ and $\boldsymbol{V_{SMA}}$ are the surface area and volume, respectively, of the SMA wires, i_{SMA} is the current flowing through the SMA wires, h is the average heat transfer coefficient and $\boldsymbol{T_{na}}$ is the ambient temperature. From (7) to (10), we obtain the following separated equations:

$$\begin{bmatrix} \dot{\epsilon} \\ \dot{T} \\ \dot{\varepsilon} \end{bmatrix} = \begin{bmatrix} \dfrac{\mu_T \frac{i_{SMA}^2 R_{SMA} - hS_{SMA}(T - T_{na})}{\rho_{SMA} V_{SMA} c_{SMA}}}{1 + \mu_\sigma k \varepsilon_L \frac{E(\epsilon)}{E(\epsilon)+k} - \mu_T \frac{H}{c_{SMA}}}, A_S + \frac{\sigma_{SMA}}{C_A} \leq T \leq A_f + \frac{\sigma_{SMA}}{C_A} \\ \dfrac{i_{SMA}^2 R_{SMA} - hS_{SMA}(T - T_{na})}{\rho_{SMA} V_{SMA} c_{SMA}} + \frac{H\dot{\epsilon}}{c_{SMA}} \\ \dfrac{E(\epsilon)\varepsilon_L}{E(\epsilon)+k}\dot{\epsilon} \end{bmatrix} \tag{11}$$

where $\boldsymbol{\mu_T} = -\boldsymbol{a_A}\frac{\epsilon_0}{2}\sin\left[\boldsymbol{a_A}\left(\boldsymbol{T} - \boldsymbol{A_s}\right) + \boldsymbol{b_A}\boldsymbol{\sigma_{SMA}}\right]$, $\boldsymbol{\mu_\sigma} = -\boldsymbol{b_A}\frac{\epsilon_0}{2}\sin[\boldsymbol{a_A}\left(\boldsymbol{T} - \boldsymbol{A_s}\right) + \boldsymbol{b_A}\boldsymbol{\sigma_{SMA}}$

3.2 Thermodynamic Simulation of the Bidirectional Flexible Bending Actuator

The reciprocating bending motion of the actuator relies on the phase transformation of SMA wires which is initiated by varying the SMA wire temperature. Recall, in our design, SMA wires are embedded into PDMS and the PDMS will be in water. Thus, heat flows from SMA wires to PDMS and then from PDMS to water. If the cooling time is long enough to ensure that SMA wires cool down, the reciprocating bending motion of the actuator can be realized. However, when the actuator is actuated at high frequency, the heat produced by SMA wires is not completely transferred to water. Such heat accumulation reduces the bending ability of the artificial muscles.

To gain more insight into the heat transfer process of the actuator, a simplified simulation model was set up in COMSOL™ Multiphysics 6.0 (Fig. 7a). Regarding the actuation of the artificial muscles, two different heating schemes (R and D) are utilized. In the D heating scheme, four SMA wires are heated at the same time, while in the R heating scheme, two SMA wires in faces A and B are heated in one actuation period, and the other two pairs of SMA wires are heated in the next period. The heating time is 200 ms and the cooling time is 100 ms. Figure 7b shows the temperature distribution of the actuator by using R (i) and D (ii) heating schemes at 0.2 s, and Fig. 7c plots the time evolution over 10 s. From the latter figure, keeping in mind that M_F = 41.4 ℃, it comes that, SMA wires cool down almost completely in the R scheme. However, in scheme D there is a huge accumulation of heat. As a result, the R heating scheme can effectively inhibit the heat accumulation problem when the artificial muscles actuate at high frequency.

Furthermore, in case of heat accumulation, SMA wires do not recover their original shape upon transformation, thus the bending range of the actuator decreases. To verify this point, we have conducted an experiment with the same conditions as those of the previous simulation. We define the bending range ratio as the ratio of the instantaneous bending range to the initial bending range (whose values are 47° and 62° in the R and D heating schemes, respectively) of the actuator. The experimental measurements of the bending ranage ratio are plotted in Fig. 8. The result is consistent with simulation one. More specifically, the bending ability of the actuator decreases very slightly in the R heating scheme, while it decays tremendously in the D heating scheme.

By heating different numbers of channels of SMA-wire with the AR control scheme, we obtain four groups of

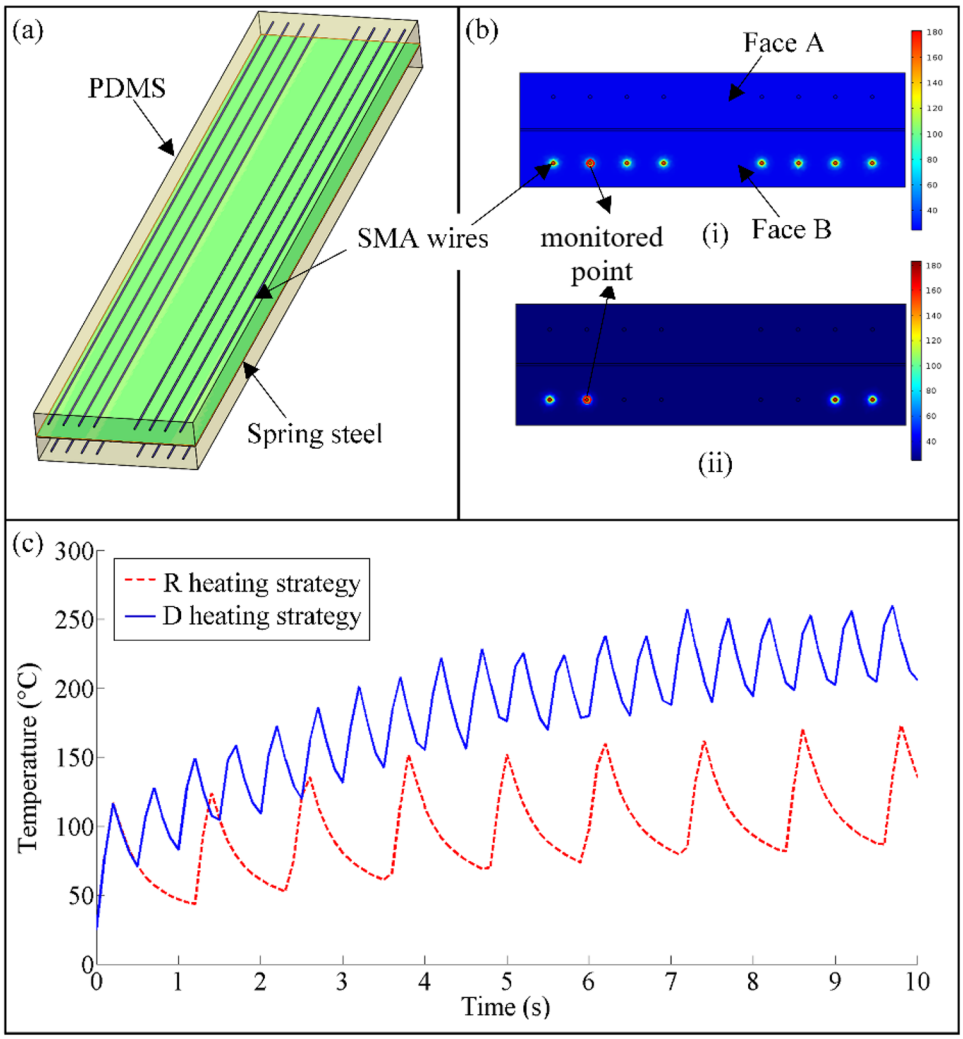

Fig. 7 Thermodynamic simulation of the actuator in COMSOL. **a** Model. **b** Temperature distribution. **c** Evolution of the temperature of a monitored point during 10 s

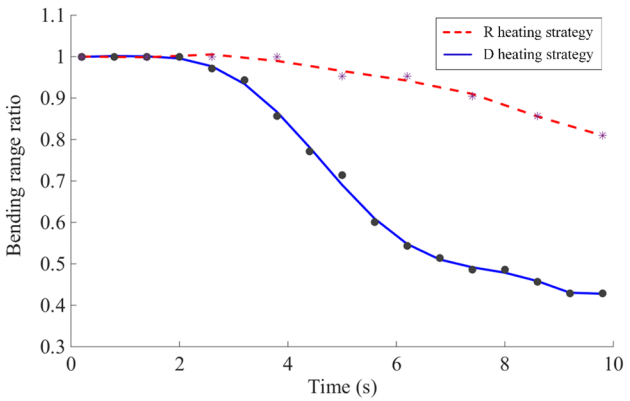

Fig. 8 Time evolution of the bending range ratio of the bi-directional flexible actuator

actuation responses (Fig. 9). When, SMA wires reach the end of the phase transformation ($\tau = 1$), the bending range is accurately known. However, for $\tau \neq 1$, i.e., SMA wires are in a thermal intermediate state, the bending range is unreliable (large error bar).

4 Locomotion Analysis and Control of SoRoFAAM-1

A large number of experiments have been performed in a rectangular tank of size $150cm \times 70cm \times 100cm$ (length × width × height) to analyse the swimming characteristics of SoRoFAAM-1 for different heating strategies of the actuator. A Nikon D800 camera was used for motion recording.

4.1 Cruise and Head Swing Factor

Recall that the artificial muscles can produce four accurate actuations based on the number of heated channels (SMA wires) with the AR heating strategy. The results of

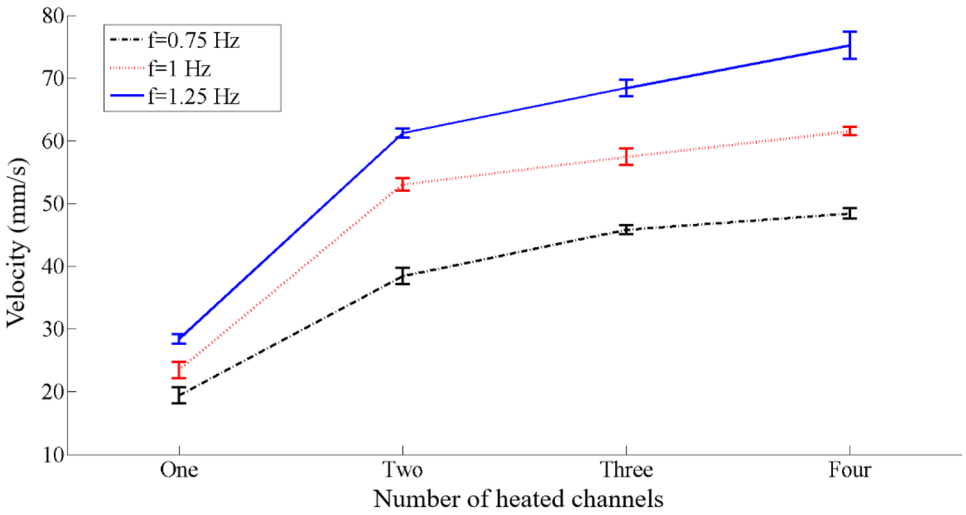

Fig. 9 Cruise velocity of SoRo-FAAM-1 as a function of the number of heated channels at several frequencies

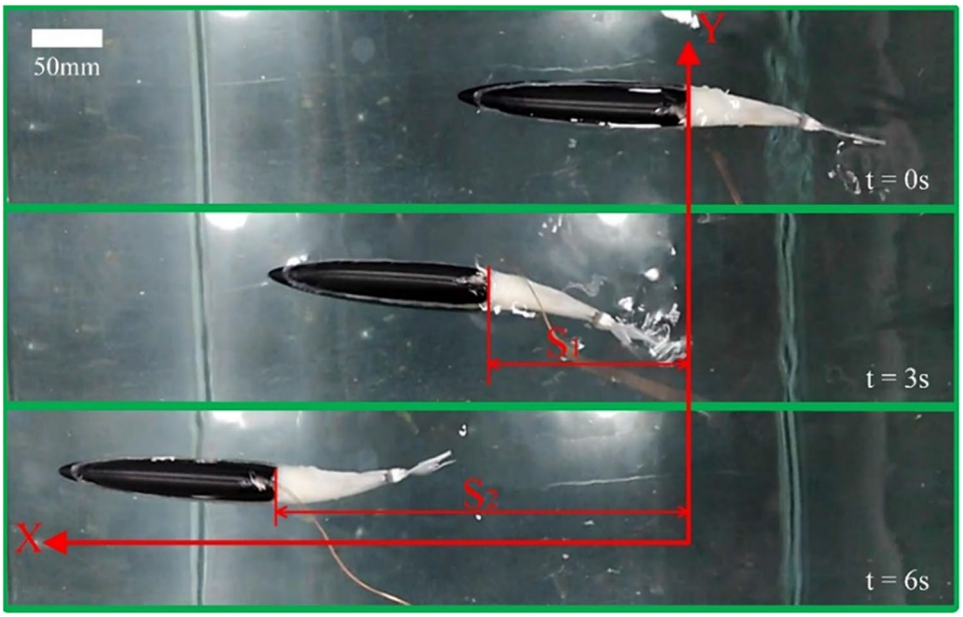

Fig. 10 Photos of SoRo-FAAM-1 during cruising at 1 Hz

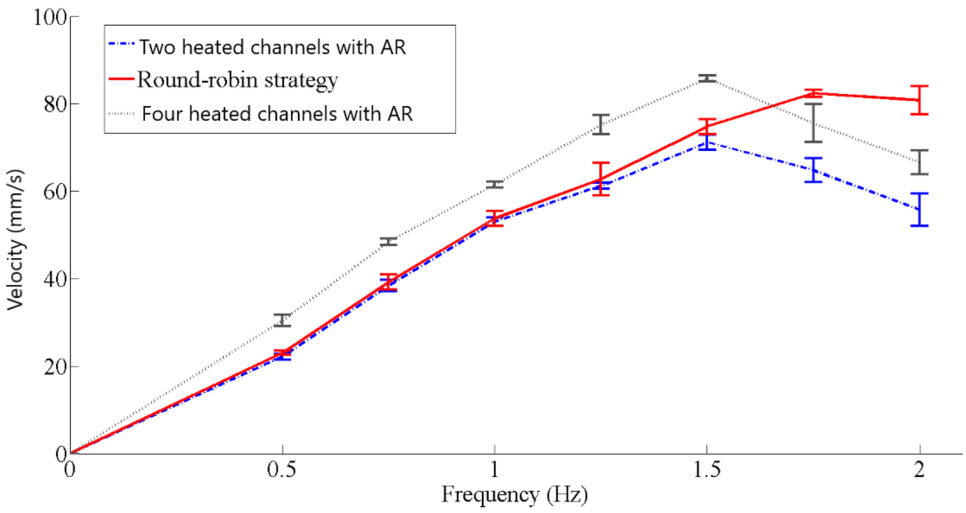

Fig. 11 Velocity of SoRo-FAAM-1 as a function of the frequency with round-robin and AR heating strategies

the experiments on the relationship between SoRoFAAM-1 cruise-velocity, the number of heated channels of SMA wire and the actuation frequency are depicted in Fig. 9. The velocity of SoRoFAAM-1 increases with both the number of heated channels and the frequency. Figure 10 shows a photo of SoRoFAAM-1 in cruise at 1 Hz by heating two channels.

The effect of the heating strategy on the velocity-frequency relationship of SoRoFAAM-1 is depicted in Fig. 11. In AR heating strategy with 2 or 4 heated channels, the speed increases gradually with frequency up to 1.5 Hz and then starts to decrease. This is due to the heat accumulation problem described in subSect. 3.2. However, in the Round-Robin strategy, presented in subsection 4.4, the velocity increases up to 2 Hz. The maximum speed of SoRoFAAM-1 in these experiments is 87 mm/s at 1.5 Hz with four heated channels.

An important nondimensional number characterizing the swimming hydrodynamics of living fish is the head swing factor (S_h). The head swing factor is defined as the ratio of the head-tip amplitude to the tail-fin amplitude, $S_h = a_h/a_t$. For living fish, S_h ranges between 0.15 and 0.40. The larger S_h is, the more inefficient swimming is. In fact, a large S_h implies an important head swing amplitude, which in turn implies both a high zig-zag-like cruise and an increase in form drag since the longitudinal cross-section thereby increases. Furthermore, additional energy dissipation occurs because of this head transverse motion, whose magnitude increases with increasing distance travel, i.e., a_h. SoRoFAAM-1, when cruising at 1.5 Hz with four heated channels, has $a_h = 17$ mm and $a_t = 45$ mm; hence, $S_h = 0.38$. Thus, the head swing factor of SoRoFAAM-1 lies within the range of those of living fish. This signifies that SoRoFAAM-1 swims like living fish.

The Strouhal number (S_t) is defined by $St = fA/U$, where U is the maximum forward velocity and f and A are the tail-beat frequency and peak-to-peak amplitude, respectively. It is an important nondimensional number in fish hydrodynamics. It measures how often tail-fin flapping is converted into propulsion. Living fish have S_t between 0.25 and 0.40. SoRoFAAM-1 has Strouhal numbers of 0.61, 0.63 and 0.64 at 0.75, 1.0 and 1.25 Hz, respectively. This discrepancy between the Strouhal number of living fish and that of SoRoFAAM-1 may be due to the additional drag and disturbance caused by surface waves, as a tiny portion of SoRoFAAM-1 is above the water surface.

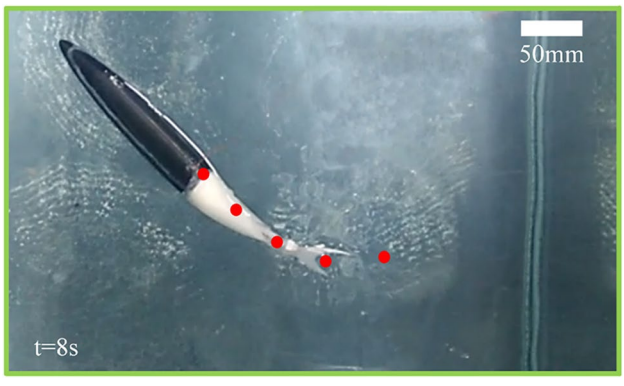

Fig. 12 Trajectory of SoRoFAAM-1 for the A3-B1 turning combination

Table 3 The curvature radius of SoRoFAAM-1 at 0.8 Hz

Face B	Face A			
	1	2	3	4
0	43 mm	138 mm	148 mm	158 mm
1	–	162 mm	203 mm	340 mm
2	–	–	3180 mm	3218 mm
3	–	–	–	$+\infty$

4.2 Turning and Maneuverability

In the previous subsection, we symmetrically actuated both artificial muscle modules to enable SoRoFAAM-1 to move straight ahead. When the actuation is asymmetric, SoRoFAAM-1 can turn (yawing). Since each artificial muscle can produce four actuations, a total of 10 groups of asymmetric combinations can be realized A1-B0, A2-B0, A3-B0, A2-B1, A3-B1, A3-B2, A4-B0, A4-B1, A4-B2 and A4-B3. In AX and BX, X represents the number of heated SMA wires in face A and face B, respectively. To analyse the yawing motion of SoRoFAAM-1, we have conducted a series of experiments at 0.8 Hz by using the AR control scheme. Figure 12 shows a photo of the motion of SoRoFAAM-1 with the A3-B1 turning combination. Tables 3 and 4 present the radius of curvature and angular velocity of SoRoFAAM-1, respectively, for the 10 turning combinations. The radius of the trajectory is an increasing function of the number of heated channels in both faces A and B. The maximum angular velocity obtained is 18°/s at 1.5 Hz using A4-B0.

Maneuverability has been intensively used in the context of underwater vehicles to characterize their ease in the change direction [1, 29–32]. Its importance in underwater locomotion, can be related to the high resistance offered

Table 4 The angular velocity of SoRoFAAM-1 at 0.8 Hz

Face B	Face A			
	1	2	3	4
0	2.1°/s	5.3°/s	6.4°/s	7.8°/s
1	–	4.5°/s	5.6°/s	6.8°/s
2	–	–	1.0°/s	1.4°/s
3	–	–	–	0

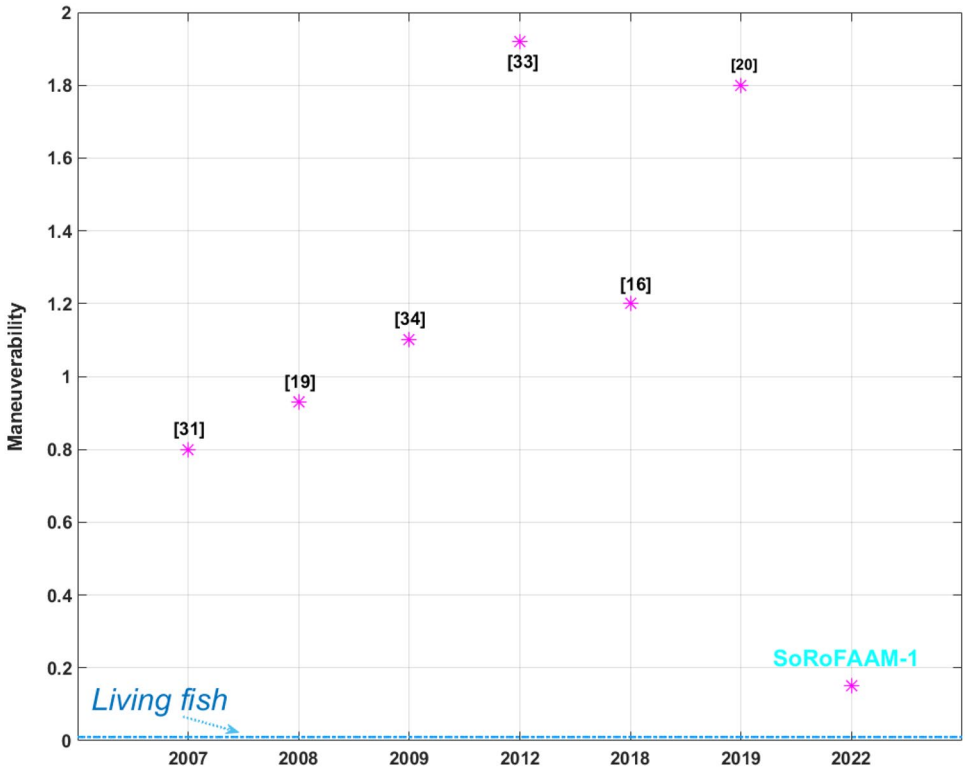

Fig. 13 Maneuverability in BCF-locomotion of soft robotic fish actuated by soft and smart materials of the literature

Table 5 Summary of the design specifications of SoRoFAAM-1

Symbol	Description	Specification	Actual value
S_h	Head Swing Factor	$0.15 \leq S_h \leq 0.4$	0.38
S_t	Strouhal Number	$0.25 \leq S_t \leq 0.4$	0.61
M_r	Maneuverability from rest	$M_r \leq 0.5$	0.15

by water compared to air. Since fish have very high maneuverability, this concept has gained significant importance in the fields of soft robotic fish as a means to compare robotic fish to living fish [1, 16, 31, 32]. In this paper, we will deal only with the maneuverability from rest. The maneuverability from rest is defined as

$$M_r = \frac{R_{\min}}{L} \tag{12}$$

where $R_{\min}$ is the smallest curvature radius and L is the length of the robotic fish. Thus, the highest maneuverability corresponds to $M \rightarrow 0$ (case of living fish). SoRoFAAM-1 has $R_{\min} = 43$ mm and $L = 280$ mm; thus $M_r = 0.15$. Figure 13 depicts the maneuverability of BCF-locomotion-based soft robotic fish with smart-material based actuators reported in the literature. However, most authors of the reviewed papers have reported neither direct nor indirect information on maneuverability. In general, BCF locomotion-based robotic fish have poor maneuveralibity compared to MPF locomotion-based robotic fish. However, we see from the Fig. 13 that SoRoFAAM-1 realizes considerable improvement in this regard (from 0.8 to 0.15). Thus, SoRoFAAM-1 is more maneuverable than previously reported BCF-locomotion-based soft robotic fish. Since, this maneuverability is close to that of living fish, SoRoFAAM-1 has a good bionic fidelity. Table 5 summarizes the design of SoRoFAAM-1.

4.3 Round-Robin Strategy

Heat accumulation is the major obstacle to achieving a high operating frequency. Based on the four bending ranges of each artificial muscle module, a new heating strategy, namely, the round-robin heating strategy, is proposed. Figure 14 shows a schematic of the round-robin heating strategy. The flapping frequency f of SoRoFAAM-1 is given as input, and the bending period T is computed as $T = 1/f$. Both artificial muscle modules of the actuator are referred to as Module-A and Module-B. The SMA wires in faces A and B are respectively denoted by Module-A-Λ and Module-B-Λ, respectively, with $\Lambda = 1, 2, 3, 4$. The channels in faces A and B are then divided into four groups. Group 1 contains Module-A-1 and Module-A-2; Group 2, Module-B-1 and Module-B-2; Group 3, Module-A-3 and Module-A-4; and Group 4 contains Module-B-3 and Module-B-4. The AR heating strategy is used to limit the

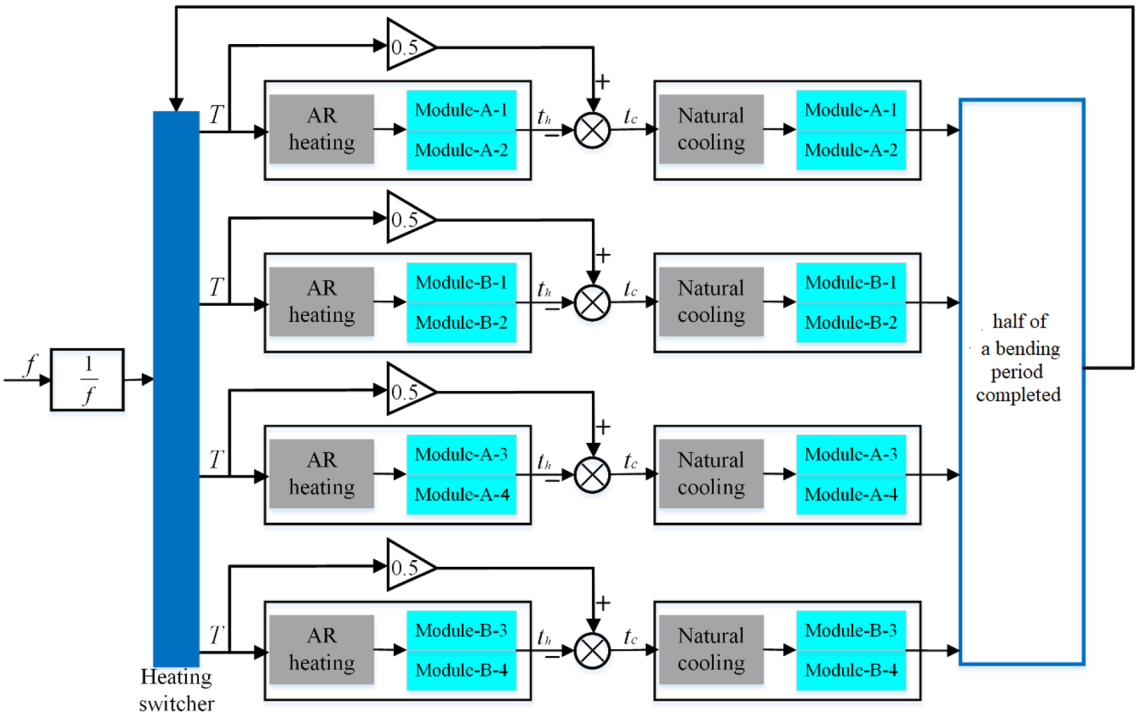

Fig. 14 Schematic of the round-robin heating strategy

heating time t_h of each group. Once the SMA wires finish the reverse martensitic transformation, they start cooling naturally. The cooling time $t_c = T/2 - t_h$. The processing sequence is successively group $1 -> $ group $2 -> $ group $3 -> $ group 4. Once half of a period is completed, the heating switcher switches to the next group to be processed.

Figure 12 plots the linear velocity of SoRoFAAM-1. The round robin strategy improves the allowed maximum frequency which is limited by heat accumulation from 1.5 Hz (in AR heating strategy) to 2 Hz. The maximum velocity is 81 mm/s in the round robin strategy.

The power dissipation by the actuator is given by $P = 2n\frac{V^2}{R} f t_{\mathrm{h}}$, where V is the supply voltage, and R is the resistance of one SMA wire. Since the resistance of one SMA wires changes slightly, we assume that R is constant and n is the number of heated SMA wires in each artificial muscle. We express the heat dissipation ratio as followed: $\delta = U/P$ where U is the velocity of SoRoFAAM-1. The maximum velocity in Fig. 11 is 87 mm/s with four heating channels at 1.5 Hz, leading to a heat-dissipation ratio $\delta_1 = 7.25 \times \frac{R}{V^2 t_h}$. The maximum speed in the round-robin strategy is 81 mm/s at 1.75 Hz; hence, $\delta_2 = 11.6 \times \frac{R}{V^2 t_h}$. Thus, $\delta_2 = 1.6\delta_1$. Therefore, the heat dissipation ratio is improved by 60% using round robin strategy.

5 Conclusions and Future Work

In this paper, we have described the design, fabrication, control and kinematics of a soft robotic fish mimicking carangiform swimmers and actuated by artificial muscles. The thermomechanical model of the actuator was derived, and the thermal transformation was analyzed numerically and experimentally. We have developed an AR strategy based on SMA wires resistance feedback. Then we have proposed a round robin heating strategy to improve the flapping frequency and heat dissipation. The kinematics of SoRoFAAM-1 has been investigated. Indeed, the maximum velocity in cruising was 87 mm/s at 1.5 Hz and in yawing was 18°/s. Our goal was to design a soft robotic fish with high bionic fidelity. This goal was specified by means of the head swing factor, the Strouhal number and the maneuverability. Out of these three specifications, two were met. The maneuverability has been satisfied with a good margin, resulting in a more maneuverable soft robotic fish than previously reported soft robotic fish using BCF locomotion. In addition, the head swing factor specification was satisfied and the obtained value lies within the range of those of living fish. Therefore, these two results show the high potential of soft and smart materials made

artificial muscles in mimicking living creatures. In our future works, we will improve the structural design and introduce pectoral fins. This should allow SoRoFAAM-2 to pitch in particular and endow it with high controllability in general. We will exploit this latter feature to design robust kinematic controllers.

Supplementary Information The online version contains supplementary material available at https://doi.org/10.1007/s42235-023-00390-6.

Acknowledgements The authors gratefully acknowledge financial support from the National Science Foundation of China (Nos. 61773358) and Cyrus Tang Foundation.

Data Availability Statement All data generated or analysed during this study are included in this published article and its supplementary materials.

Declarations

Conflict of interest The authors have no conflicts of interest to disclose.

References

1. Raj, A., & Thakur, A. (2016). Fish-inspired robots: Design, sensing, actuation, and autonomy-a review of research. *Bioinspiration & Biomimetics., 11*, 031001.
2. Du, R., Li, Z., Youcef-Toumi, K., Alvarado, y Alvarado, P. V., (eds) (2015). *Robot fish : Bio-inspired fishlike underwater robots*. Springer-Verlag Berlin Heidelberg (pp. 5–7). https://doi.org/10.1007/978-3-662-46870-8
3. Sfakiotakis, M., Lane, D. M., & Davies, J. B. C. (1999). Review of fish swimming modes for aquatic locomotion. *IEEE Journal of Oceanic Engineering, 24*, 237–252. https://doi.org/10.1109/48.757275
4. Lauder, G. V. (2009). Swimming hydrodynamics: Ten questions and the technical approaches needed to resolve them. *Experiments in Fluids, 51*(1), 23–35. https://doi.org/10.1007/s00348-009-0765-8
5. Stefanini, C., Orofino, S., Manfredi, L., Marrazza, S., Assaf, T., Capantini, L., Sinibaldi, E., Grillner, S., Wallén, P., & Dario, P. (2012). A novel autonomous, bioinspired swimming robot developed by neuroscientists and bioengineers. *Bioinspiration & Biomimetics, 7*, 025001. https://doi.org/10.1088/1748-3182/7/2/025001
6. Matthews, D., & Lauder, G. V. (2021). Fin–fin interactions during locomotion in a simplified biomimetic fish model. *Bioinspiration & Biomimetics, 16*, 046023. https://doi.org/10.1088/1748-3190/ac03a8
7. Wolf, Z., Jusufi, A., Vogt, D. M., & Lauder, G. V. (2020). Fish-like aquatic propulsion studied using a pneumatically-actuated soft-robotic model. *Bioinspiration & Biomimetics, 15*, 046008. https://doi.org/10.1088/1748-3190/ab8d0f
8. Berlinger, F., Saadat, M., Haj-Hariri, H., Lauder, G. V., & Nagpal, R. (2021). (2021) Fish-like three-dimensional swimming with an autonomous, multi-fin, and biomimetic robot. *Bioinspiration & Biomimetics, 16*, 026018. https://doi.org/10.1088/1748-3190/abd013
9. Rao, A., Srinivasa, A. R., & Reddy, J. N. (2015). Design of shape memory allow (SMA) actuators. *Springer Briefs in Computational Mechanics*. https://doi.org/10.1007/978-3-319-03188-0
10. Shintake, J., Cacucciolo, V., Shea, H. R., & Floreano, D. (2018). Soft biomimetic fish robot made of dielectric Elastomer actuators. *Soft Robotics, 5*, 466–474.
11. Jin, H., Dong, E., Xu, M., Liu, C., Alici, G., & Jie, Y. (2016). Soft and smart modular structures actuated by shape memory alloy (SMA) wires as tentacles of flexible robots. *Smart Materials and Structures, 25*, 085026.
12. Ye, Z., Hou, P., & Chen, Z. (2017). 2D maneuverable robotic fish propelled by multiple ionic polymer–metal composite artificial fins. *International Journal of Intelligent Robotics and Applications, 1*, 195–208.
13. Hubbard, J., Fleming, M., Palmre, V., Pugal, D., Kim, K., & Leang, K. (2014). Monolithic IPMC fins for propulsion and maneuvering in bioinspired underwater robotics. *IEEE J Oceanic Engineering, 39*, 540–551.
14. Zhang, Z., Yang, T., Zhang, T., Zhou, F., Cen, N., Li, T., & Xie, G. (2020). Global vision-based formation control of soft robotic fish swarm. *Soft Robotics*. https://doi.org/10.1089/soro.2019.0174
15. Li, T., Li, G., Liang, Y., Cheng, T., Dai, J., Yan, X., Liu, B., Zeng, Z., Huang, Z., Luo, Y., Xie, T., & Yang, W. (2017). Fast-moving soft electronic fish. *Science Advances*. https://doi.org/10.1126/sciadv.1602045
16. Berlinger, F., Duduta, M., Gloria, H., Clarke, D. R., Negal, R., Wood, R. J. (2018). A modular dielectric elastomer actuator to drive miniature autonomous underwater vehicles. In: *IEEE International Conference on Robotics and Automation* (IEEE) (ICRA 2018) (pp. 3429–3435). IEEE
17. Feng, H., Sun, Y., Todd, P. A., & Lee, H. P. (2019). Body wave generation for anguilliform locomotion using a fiber-reinforced soft fluidic elastomer actuator array toward the development of the eel-inspired underwater. *Soft Robotics, 7*, 233–250. https://doi.org/10.1089/soro.2019.0054
18. Marchese, A. D., Onal, C. D., & Rus, D. (2014). Autonomous soft robotic fish capable of escape maneuvers using fluidic elastomer actuators. *Soft Robotics, 1*, 75–87.
19. Wang, Z., Hang, G., Li, J., Wang, Y., & Xiao, K. (2008). A micro-robot fish with embedded SMA wire actuated flexible biomimetic fin. *Sensors Actuators A, 144*, 354–360. https://doi.org/10.1016/j.sna.2008.02.013
20. Shaw, H., & Thakur, A. (2019). Shape memory alloy based caudal fin for a robotic fish: Design, fabrication, control and characterization. *Proceedings of the Advances in Robotics, 56*, 1–6. https://doi.org/10.1145/3352593.3352666
21. Lagoudas, D. C. (ed). (2008). *Shape memory alloys modeling and engineering applications* (pp. 1–51). Springer US
22. Laschi, C., & Cianchetti, M. (2014). Soft robotics: New perspectives for robot bodyware and control. *Frontiers in Bioengineering and Biotechnology, 2*, 3. https://doi.org/10.3389/fbioe.2014.00003

23. Elahinia, M., & Ashrafiuon, H. (2002). Nonlinear control of a shape memory alloy actuated manipulator. *Journal of Vibration and Acoustics, 124*, 566. https://doi.org/10.1115/1.1501285
24. Rossi, C., Colorado, J. D., Coral, W., & Barrientos, A. (2011). Bending continuous structures with SMAs: a novel robotic fish design. *Bioinspiration & Biomimetics, 6*, 045005. https://doi.org/10.1088/1748-3182/6/4/045005
25. Ma, N., & Song, G. (2003). Control of shape memory alloy actuator using pulse width modulation. *Smart Materials and Structures, 12*, 712–719. https://doi.org/10.1088/0964-1726/12/5/007
26. Ma, N., Song, G., & Lee, H. J. (2004). Position control of shape memory alloy actuators with internal electrical resistance feedback using neural networks. *Smart Materials and Structures, 13*, 777–783. https://doi.org/10.1088/0964-1726/13/4/015
27. Jin, H., Dong, E., Alici, G., Shixin, M., Xu, M., Chunshan, L., & Kin, L. H. (2016). A starfish robot based on soft and smart modular structure (SMS) actuated by shape memory alloy wires. *Bioinspiration & Biomimetics, 11*, 056012.
28. Liang, C., & Rogers, C. A. (1990). One-dimensional thermomechanical constitutive relations for shape memory materials. *Journal of Intelligent Material Systems and Structures, 1*, 207–234.
29. Bandyopadhyay, P. R. (2005). Trends in biorobotic autonomous undersea vehicles. *IEEE Journal of Oceanic Engineering, 30*, 109–139.
30. Bandyopadhyay, P. R., Castano, J. M., Rice, J. Q., Philips, R. B., Nedderman, W. H., & Macy, W. K. (1997). Low-speed maneuvering hydrodynamics of fish and small underwater vehicles. *ASME Journal of Fluids Engineering, 119*, 136–144.
31. Ye, X., Su, Y., Guo, S. (2007). A centimeter-scale autonomous robotic fish actuated by IPMC actuator. In: *IEEE International Conference on Robotics and Biomimetics* 2007 (ROBIO 2007) (pp. 262–267). IEEE
32. Berlinger, F., Dusek, J., Gauci, M., & Nagpal, R. (2018). Robust maneuverability of a miniature low-cost underwater robot using multiple fin actuation. *IEEE Robotics and Automation Letters, 3*, 140–147.
33. Kim, S. H., Shin, K., Hashi, S., & Ishiyama, K. (2012). Magnetic fishrobot based on multi-motion control of a flexible magnetic actuator. *Bioinspiration & Biomimetics, 7*, 036007. https://doi.org/10.1088/1748-3182/7/3/036007
34. McGovern, S., Alici, G., Truong, V. T., & Spinks, G. M. (2009). Finding NEMO (novel electromaterial muscle oscillator): a polypyrrole powered robotic fish with real-time wireless speed and directional control. *Smart Materials and Structures, 18*, 095009. https://doi.org/10.1088/0964-1726/18/9/095009